PHYSICAL REVIEW B **79**, 104113 (2009)

Structural changes underlying the diffuse dielectric response in $AgNbO_3$

Igor Levin,[1] Victor Krayzman,[1] Joseph C. Woicik,[1] Jenia Karapetrova,[2] Thomas Proffen,[3]
Matthew G. Tucker,[4] and Ian M. Reaney[5]
[1]*Ceramics Division, National Institute of Standards and Technology, Gaithersburg, Maryland 20899, USA*
[2]*Advanced Photon Source, Argonne National Laboratory, Argonne, Illinois 60439, USA*
[3]*Lujan Neutron Center, Los Alamos National Laboratory, Los Alamos, New Mexico 87545, USA*
[4]*ISIS, Rutherford Appleton Laboratory, Didcot OX11 0OX, United Kingdom*
[5]*Department of Engineering Materials, University of Sheffield, Sheffield S1 3JD, United Kingdom*
(Received 26 January 2009; revised manuscript received 23 February 2009; published 26 March 2009)

Structural differences in the so-called M polymorphs of $AgNbO_3$ were analyzed using combined high-resolution x-ray diffraction, neutron total scattering, electron diffraction, and x-ray absorption fine-structure measurements. These polymorphs all crystallize with *Pbcm* symmetry and lattice parameters $\sqrt{2}a_c \times \sqrt{2}a_c \times 4a_c$ (where $a_c \approx 4$ Å corresponds to the lattice parameter of an ideal cubic perovskite) which are determined by a complex octahedral tilt system $(a^-b^-c^-)/(a^-b^-c^+)$ involving a sequence of two *in-phase* and two *antiphase* rotations around the *c* axis. Our results revealed that, similar to $KNbO_3$, the Nb cations in $AgNbO_3$ exhibit local off-center displacements correlated along Nb-Nb-Nb chains. The displacements appear to be present even in the high-temperature $AgNbO_3$ polymorphs where the Nb cations, on average, reside on the ideal fixed-coordinate sites. The onset of the $(a^-b^-c^-)/(a^-b^-c^+)$ tilting in the M polymorphs lifts the symmetry restrictions on the Nb positions and promotes ordering of the local Nb displacements into a long-range antipolarlike array. This ordering preserves the average *Pbcm* symmetry but is manifested in electron diffuse scattering and corroborated by other local-structure sensitive techniques. Structural states previously identified as the M_3 and M_2 phases represent different stages of displacive ordering rather than distinct thermodynamic phases. Rietveld refinements indicated intimate coupling between the displacive behavior on the oxygen, Nb, and Ag sublattices. The *Pbcm* symmetry of the octahedral framework precludes a complete ordering of Nb displacements so that some positional disorder is retained. This partial disorder likely gives a source to the dielectric relaxation which, according to previous spectroscopic studies, is the origin of the diffuse dielectric response exhibited by M-type $AgNbO_3$ at ≈250 °C.

DOI: 10.1103/PhysRevB.79.104113 PACS number(s): 61.50.Ks, 61.05.cp, 61.05.F−, 61.05.J−

I. INTRODUCTION

$AgTa_xNb_{1-x}O_3$ perovskite solid solutions exhibit a rare combination of high but temperature stable dielectric constants and modest dielectric losses which renders them attractive candidates for high-frequency capacitors.[1,2] Despite the technological importance of these materials, the structural origin of their high dielectric constants remains uncertain. Moreover, even the details of the crystal structures and phase transitions among the polymorphs of the end-compound $AgNbO_3$ remain a subject of debate.

At room temperature, $AgNbO_3$ crystallizes with a perovskite-related structure[3] that exhibits orthorhombic symmetry (*Pbcm*) and lattice parameters $\sqrt{2}a_c \times \sqrt{2}a_c \times 4a_c$ ($a_c \approx 4$ Å corresponds to an ideal cubic perovskite). This superstructure (Fig. 1) features a so-called compound tilting of $[NbO_6]$ octahedra described in Glazer's notation[4] as $(a^-b^-c^-)/(a^-b^-c^+)$. A sequence of two *in-phase* and two *antiphase* octahedral rotations about the *c* axis yields a $4a_c$ periodicity with the two crystallographically distinct Ag sites, Ag1 and Ag2. In addition to tilting, the $AgNbO_3$ structure exhibits concerted off-center Ag and Nb displacements that adopt the symmetry of the tilted octahedral framework (Fig. 2). The Nb and Ag1 displacements are directed preferentially along the *b* axis whereas the Ag2 displacements occur parallel to the *a* axis. Similar octahedral-tilting and cation displacements are encountered in $NaNbO_3$ (Refs. 5 and 6) and $Ca_{1-x}Sr_xTiO_3$ (x=0.59–0.65).[7,8]

Upon heating, $AgNbO_3$ has been reported to undergo a series of at least five reversible structural phase transitions (Fig. 3) that involve different types of octahedral rotations and cation displacements.[9–11] The transitions $M_3 \leftrightarrow O$,

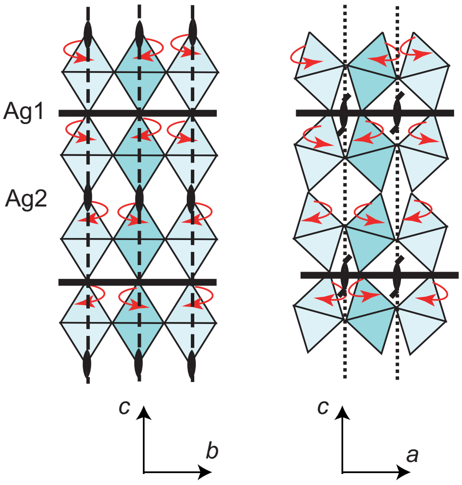

FIG. 1. (Color online) Schematics of the octahedral framework in the M-phase structure of $AgNbO_3$ with the symmetry elements superimposed. Octahedral rotations about the *c* axis are indicated using arrows. Ag1 and Ag2 specify *c* planes occupied by the symmetrically nonequivalent Ag cations.

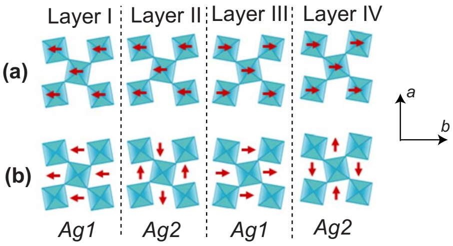

FIG. 2. (Color online) Schematics of the Nb (a) and Ag (b) displacements in the successive *c* layers (I, II, III, and IV) within the *Pbcm* structure (Fig. 1). The displacement directions are indicated using arrows.

O↔T, and T↔C arise from octahedral-tilting instabilities and as such are considered to be well understood (Fig. 3). In contrast, the transitions among the M phases have been attributed to cation displacements; however, their exact nature has not been clarified. The transition of most practical and fundamental interest is the $M_2 \leftrightarrow M_3$, which is manifested by a diffuse maximum in the temperature dependence of dielectric constant.[1] Studies using dielectric spectroscopy have attributed this peak to a submillimeter Nb relaxational mode.[12,13] In $AgNb_{1-x}Ta_xO_3$ solid solutions, the $M_2 \leftrightarrow M_3$ transition temperature decreases with increasing Ta content so that for $x = \frac{1}{2}$ the maximum of dielectric constant occurs in the exploitable room-temperature range.[1,2]

The $M_2 \leftrightarrow M_3$ diffuse transition reportedly causes an abrupt splitting of the 004_c reflections in x-ray diffraction patterns below the transition temperature.[9–11] Yet, recent structural refinements of $AgNbO_3$ using powder neutron-diffraction data[11] revealed no changes in the average symmetry (*Pbcm*) across the transition, which suggests that the structural changes are subtle and may involve correlations among atomic displacements over a limited spatial scale.

In the present study, we combined x-ray and neutron powder diffraction (including total neutron scattering), extended x-ray absorption fine-structure (EXAFS) measurements, and transmission electron microscopy to elucidate the nature of the structural changes in the so-called M-phase polymorphs of $AgNbO_3$.

II. EXPERIMENT

$AgNbO_3$ samples were prepared using conventional solid-state synthesis by heating a mixture of Ag_2O (c. p. grade) and Nb_2O_5 (99.9985%) at 850 °C for 5 h under flowing oxygen. The mixture contained a 3 wt % (Ref. 14) excess of Ag_2O to compensate for a loss of Ag during thermal exposure. Samples were mixed under acetone using an agate mortar and pestle for 20 min, dried, and pressed into a pellet. For synthesis, the pellet was placed on a bed of sacrificial powder on Pt foil and covered with a ZrO_2 crucible. A separate Pt container filled with Ag_2O powder was placed inside this crucible next to the sample to provide a silver-rich atmosphere. The resulting bright-yellow powder contained phase-pure $AgNbO_3$, as confirmed by x-ray diffraction.

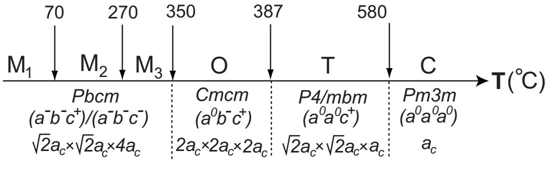

FIG. 3. Sequence of the reported phase transitions in $AgNbO_3$.

X-ray diffraction patterns for assessment of sample purity and for Rietveld refinements were collected using a high-resolution powder diffractometer equipped with a Ge incident-beam monochromator (Cu $K\alpha_1$ radiation) and a linear position sensitive detector. Variable-temperature x-ray diffraction measurements were conducted on the 33-BM beamline at the Advanced Photon Source. One set of experiments was performed on selected reflections using an analyzer crystal in the diffracted beam path. For these experiments, the sample powder was dispersed in ethanol and deposited on a thin (15 μm) Al foil which was mounted on the Linkam heating stage. Data were collected in transmission using an incident x-ray beam energy of 20 keV; the stage was rocked with an amplitude of ±0.5° to improve powder averaging. Diffraction patterns for Rietveld refinements were collected using the same diffractometer but without an analyzer crystal. For these measurements, the sample was packed in a 0.5 mm quartz capillary and mounted in a custom high-temperature furnace. The diffraction patterns were collected in transmission at an energy of 17 keV ($\lambda = 0.7388$ Å) up to $Q = 8$ Å^{-1}. The capillary was spun during data collection. The raw data were corrected for absorption and analyzed using the GSAS software package.[15]

Variable-temperature Nb and Ag *K*-edge EXAFS measurements were conducted at the NIST X23A2 beamline of the National Synchrotron Light Source. The double-crystal monochromator was operated with a pair of Si (311) crystals. Data were collected in transmission using the same Linkam temperature stage and sample mounting as described for the x-ray diffraction experiments. Three spectra were collected at each temperature. For several temperatures, the spectra were first collected on heating and then recollected on cooling; the data proved to be highly reproducible. All spectra were processed using the Athena code.[16] Local-structure models were refined by fitting the EXAFS signal calculated with the FEFF8.20 code[17] to the experimental data. A self-consistent potential was used in the FEFF calculations. The fitting was accomplished using the ARTEMIS software.[16] The Nb and Ag data were fitted simultaneously to reduce the number of independent structural variables.

Transmission electron microscopy (TEM) was performed at 200 kV. TEM samples were prepared both by dispersing the powder on lacey carbon-coated copper grids and by mechanical polishing of sintered (at 900 °C) pellets followed by ion-thinning until perforation. Ion thinning was accomplished in a Precision Ion Polishing System (PIPS) using an Ar ion-beam energy of 4 kV and an incident-beam angle of 4.5°; these relatively mild ion-thinning conditions were necessary to prevent precipitation of metallic Ag in the sample.

Variable-temperature neutron-diffraction measurements were conducted on the NPDF diffractometer at the Lujan Neutron Scattering Center (Los Alamos National Laboratory) and on the GEM diffractometer at ISIS (Rutherford

Appleton Laboratory). In both cases, the sample powder was loaded in vanadium containers. Temperature control was achieved using either a closed-cycle refrigerator (NPDF) or a high-temperature furnace (GEM). High neutron absorption by Ag (absorption cross section 63.3 b) complicated the structural refinements of AgNbO$_3$, limiting the accuracy of the atomic displacement parameters (ADP). The problem is also significant for the analyses of atomic pair-distribution functions (PDF) because large absorption corrections affect background subtraction and normalization of the total scattering data. Rietveld reciprocal-space refinements using absorption-corrected data collected at similar temperatures on the NPDF and GEM instruments yielded comparable (±2 e.s.d.—estimated standard deviation) values for all structural parameters. Here, we present only the refinements obtained using the GEM diffractometer because more temperatures were sampled during that experiment. For the PDF analyses, the NDPF data were preferred because the NPDF setup enabled a more robust background subtraction for the highly absorbing sample. Raw total scattering data were processed using the PDFGETN software to extract the PDF. A $Q_{\max}=35$ Å^{-1} was used in the Fourier transform. The PDFGUI (Ref. 18) and RMCPROFILE (Ref. 19) software packages were used for local-structure refinements.

The transition temperatures identified by the different techniques varied somewhat (±10 °C) because of the instrumental differences in the sample-heating systems. Therefore, all temperatures reported in this work are considered to be approximate (±10 °C).

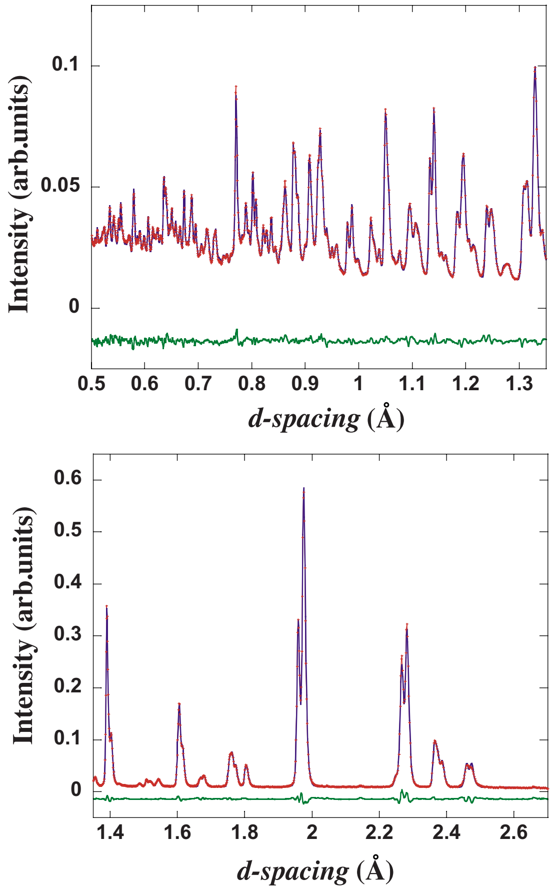

FIG. 4. (Color online) Experimental (red) and calculated (blue) neutron-diffraction profiles for AgNbO$_3$ at room temperature ($R_{\mathrm{wp}}=3.24\%$)

III. RESULTS

A. Room-temperature structure

Room-temperature x-ray, neutron, and electron-diffraction patterns of AgNbO$_3$ can be readily accounted for by the previously reported 40-atom unit cell having lattice parameters $a=5.55358(4)$ Å, $b=5.60858(4)$ Å, $c=16.6540(1)$ Å (x-ray diffraction data). Our Rietveld refinements using both neutron and x-ray diffraction data confirmed the *Pbcm* structure (Fig. 4). Neutron refinements yielded typical ADP values for all sites except the most symmetric Ag2 and O5 positions which acquired abnormally large U_{22} components (Tables I and II; Fig. 5). Refinements using x-ray diffraction also corroborated large U_{22} values for Ag2. Apparently, both the Ag2 and O5 sites exhibit displacive disorder along the *b* axis. Since these atoms reside in the same *c* planes and are nearest neighbors, their local displacements are expected to be correlated. The Ag2 cations appear to be unstable in the (3+6+3) coordination imposed by the local $(a^-b^-b^-)$-like tilting and are displaced toward the O5 atoms to acquire a $\approx[(3+1)+5+3]$ distribution of the Ag-O distances, as is observed for the Ag1 sites.

Electron-diffraction patterns (Fig. 6) displayed sharp superlattice reflections associated with octahedral-tilting and cation displacements; the reflection conditions were consistent with space group *Pbcm*. Additionally, electron diffraction revealed pronounced diffuse scattering concentrated on the $(00l)_c$ reciprocal-lattice planes (relplanes) passing through all fundamental reflections perpendicular to the *c* axis (Fig. 7). Some detectable but substantially weaker diffuse intensity was also observed on the $(h00)_c$ and $(0k0)_c$ relplanes perpendicular to the *a* and *b* axis, respectively. The diffuse scattering was extinct for the $\{00l\}_c$ relplanes passing through the origin. Similar diffuse scattering has been reported for several perovskite systems,[20,21] including orthorhombic BaTiO$_3$ and KNbO$_3$, where it was attributed to correlated B-cation displacements within linear -B-B-B- $[001]_c$ chains. The correlated displacement components within each chain (Fig. 8) must be parallel to the chain direction to account for the extinction of diffuse scattering through the origin.[21,22] A continuous distribution of diffuse intensity within the relplanes indicates the absence of transverse interchain correlations. Superposition of the average $[110]_c$ and local $[001]_c$ displacements is consistent with the assumption that the Nb cations are disordered among the two sites displaced approximately along the $[111]_c$ and $[11\bar{1}]_c$ directions (Fig. 8), as observed indeed for the orthorhombic forms of BaTiO$_3$ and KNbO$_3$.[20] This interpretation of the electron-diffraction data for AgNbO$_3$ is supported by our PDF and EXAFS measurements, as described below.

The atomic pair-distribution function for AgNbO$_3$ obtained from total neutron scattering displays a well-resolved double peak for the Nb-O nearest-neighbor distances, R_1 and R_2, instead of a single broad peak expected for the average structure [Figs. 9(a) and 9(b)]. The experimental Nb-O dis-

TABLE I. Room-temperature atomic coordinates and equivalent isotropic displacement parameters (Å^2) for the *Pbcm* structure of $AgNbO_3$ obtained from refinements using neutron powder-diffraction data (Fig. 4). Values of the refined anisotropic displacement parameters are summarized in Table II. Note: Lattice parameters $a=5.55165(4)$ Å, $b=5.60804(5)$ Å, and $c=15.6503(1)$ Å. Space group *Pbcm* (No. 57). The anisotropic displacements parameters for the oxygen sites O6 and O7 were constrained to be equal.

Atom	Site	x	y	z	$U_{eq}\times 100$
Ag1	4*d*	0.7574(6)	0.2332(3)	0.75	0.76
Ag2	4*c*	0.7567(7)	0.25	0.5	1.58
Nb	8*e*	0.7456(4)	0.7244(1)	0.6258(2)	0.52
O4	4*d*	0.7008(5)	0.7636(3)	0.75	0.49
O5	4*c*	0.8113(5)	0.75	0.5	1.16
O6	8*e*	0.4689(2)	0.5351(2)	0.6109(1)	0.82
O7	8*e*	0.9672(1)	0.4714(2)	0.6386(1)	0.82

tance distribution can be satisfactorily fitted using a double-Gaussian profile with $R_1=1.907(1)$ Å and $R_2=2.116(1)$ Å. The corresponding Debye-Waller (D-W) factors are $\sigma_1^2=0.005(1)$ Å^2 and $\sigma_2^2=0.007(1)$ Å^2. The area ratio for these two peaks is 3.3/2.7 which is consistent with local Nb displacements approximately along the $\langle 111\rangle_c$ directions. In contrast, the PDF simulated for the average-structure model obtained from conventional Rietveld refinements features a single broad Nb-O peak at $R\approx 2$ Å [Fig. 9(b)]. Real-space refinements over a local distance range could reproduce the double-peak Nb-O distribution [Fig. 9(c)] but only by modifying the anisotropy of the Nb ADP to yield a large U_{33} displacement component. This result is consistent with the model inferred from the electron-diffraction data (Fig. 8). The EXAFS-derived Nb-O peak (Fig. 10) also can be fitted assuming a double-shell (3+3) Nb coordination; attempts to describe this peak using a single-shell coordination produced a significantly worse fit (Fig. 11). The Nb-O distances, $R_1=1.905(4)$ Å and $R_2=2.108(6)$ Å and their associated Debye-Waller factors, $\sigma_1^2=0.004(1)$ and $\sigma_2^2=0.007(1)$ obtained from EXAFS are similar to those derived from the neutron PDF.

Thus, electron diffraction, neutron PDF, and EXAFS all indicate that the local coordination of Nb is different from that described by the average model. The data are consistent with local displacements of Nb along the $\langle 11\pm l\rangle_c$ directions ($l\leq 1$) so that, on average, Nb atoms are displaced along the b axis parallel to $[110]_c$; the z axis components of local displacements are correlated along the $[001]_c$ direction (Fig. 8). The alternating strong/weak intensities of the $(00l)_c$ diffuse sheets with l=odd and l=even [e.g., Fig. 7(d)] suggest the coexistence of both positive Nb-Nb and negative Nb-O displacement correlations within the $[001]_o$ (subscript "*o*" refers to the orthorhombic $\sqrt{2}a_c\times\sqrt{2}a_c\times 4a_c$ unit cell) Nb-O-Nb-O chains,[21,22] as was confirmed by our computer simulations of the diffuse scattering.

B. Structural transitions

In the present study we focused on the alleged $M_1\leftrightarrow M_2\leftrightarrow M_3$ transitions. As mentioned in Sec. I, the transitions $M_3\leftrightarrow O\leftrightarrow T\leftrightarrow C$ are generally well understood and are associated with modification of the octahedral tilt system (Fig. 3). The $M_3\rightarrow O$ transition is manifested in abrupt changes in the orthorhombic lattice distortion and the disappearance of the superlattice reflections $hk\frac{1}{4}l_c$. In the O-phase, all Nb cations reside on the ideal fixed-coordinate positions, whereas Ag atoms occupy two nonequivalent sites having variable y coordinates.

1. Diffraction Studies

In situ heating/cooling electron-diffraction experiments confirmed that the reflection conditions resulting from the symmetry glide planes b and c in the *Pbcm* space group are

TABLE II. Room-temperature anisotropic displacement parameters (×100, Å^2) for the *Pbcm* structure of $AgNbO_3$ obtained from refinements using neutron powder-diffraction data.

Atom	U_{11}	U_{22}	U_{33}	U_{12}	U_{13}	U_{23}
Ag1	0.9(1)	0.36(8)	1.0(1)	−0.11(6)	0	0
Ag2	1.0(1)	3.1(1)	0.6(1)	0	0	−0.08(7)
Nb	0.21(2)	0.56(3)	0.78(2)	0.06(4)	−0.05(3)	0.16(5)
O4	1.15(9)	0.5(1)	0.005[a]	−0.29(5)	0	0
O5	1.1(1)	2.2(1)	0.1(1)	0	0	−0.25(8)
O6, O7[b]	0.61(2)	0.73(2)	1.12(2)	−0.08(4)	−0.33(4)	−0.001(2)

[a] The U_{33} component for the O4 site was kept fixed because unconstrained refinements of this parameter produced a small negative number.

[b] The displacement parameters for the O6 and O7 sites were constrained to be equal.

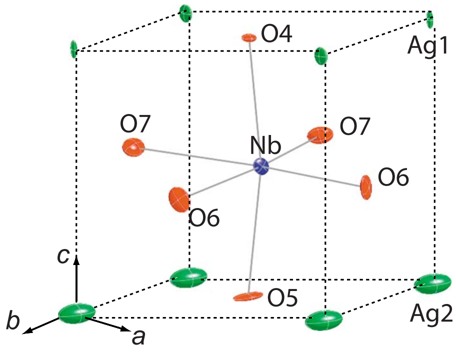

FIG. 5. (Color online) Schematic of anisotropic atomic displacement parameters (70% probability) as obtained from Rietveld refinements using room-temperature neutron-diffraction data. Note the highly anisotropic displacements for Ag2 and O5 sites.

closely obeyed up to the M↔O transition. Therefore, the *average* displacement patterns for both Ag and Nb (Fig. 2) must be maintained across the entire M-phase field. The presence of mirror planes perpendicular to the *c* axis (Fig. 1) could not be ascertained because the high incidence of twin and antiphase domain boundaries (Fig. 12) precluded the reliable use of convergent beam electron diffraction.

As found in previous x-ray diffraction studies, the $002_c = 220_o + 008_o$ reflection appeared as a single peak in the range ≈275 to ≈325 °C, but split into two peaks for $T<275$ °C—a change that has been identified[9–11] as the $M_3 \leftrightarrow M_2$ transition [Fig. 13(a)]. However, analyses of the 220_o and 008_o d spacings calculated from the lattice parameters obtained using Rietveld refinements indicate that these reflections remain split across the entire M-phase field up to the $M_3 \leftrightarrow O$ transition at ≈360 °C [Fig. 13(b)]. Thus, the previous inference of the $M_3 \leftrightarrow M_2$ transition from a seemingly "abrupt $220_o/008_o$ splitting" at ≈275 °C was misleading; instead, the temperature dependencies of the 220_o and 008_o d spacings coincidentally intersected at this temperature as seen in Fig. 13(b). Nevertheless, detailed examination of

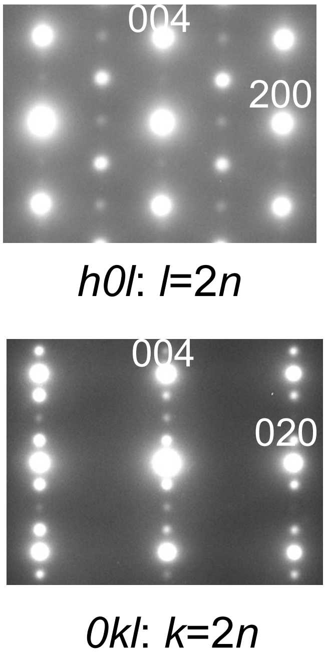

FIG. 6. Representative low-index selected area electron-diffraction patterns from $AgNbO_3$. The reflection conditions are consistent with the *b* and *c* glide planes as encountered in the *Pbcm* structure.

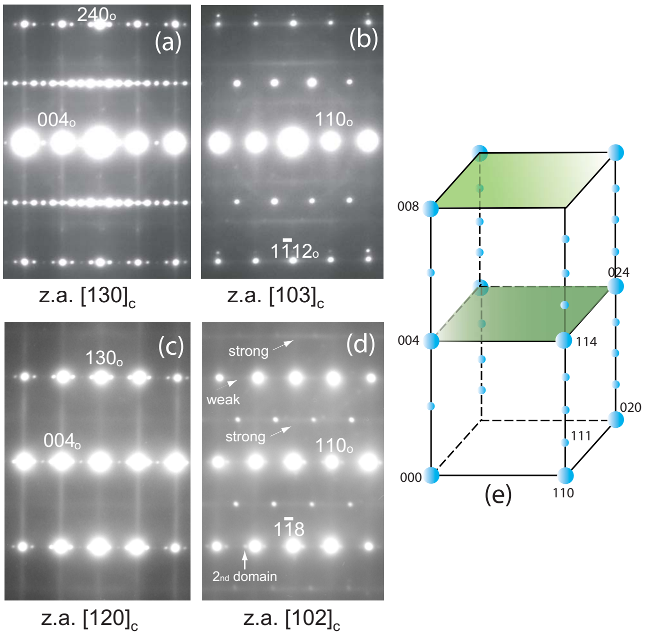

FIG. 7. (Color online) Electron-diffraction patterns recorded from a single domain of $AgNbO_3$ at room temperature. Fundamental reflections are indexed according to the $\sqrt{2}a_c \times \sqrt{2}a_c \times 4a_c$ unit cell. Note the diffuse-scattering streaks that represent intersections of the $(00l)_o$ sheets (illustrated in the drawing on the right) and the Ewald sphere. The diffuse scattering through the origin is extinct. The diffraction pattern recorded in the $[102]_c$ orientation contains a minor contribution from the second domain with a perpendicular orientation of the *c* axis. A systematic alternation (i.e., weak/strong) of diffuse intensity is observed for the streaks at $g=[112]_c$ and $g=\frac{1}{2}[112]_c$ (z.a. $[102]_c$).

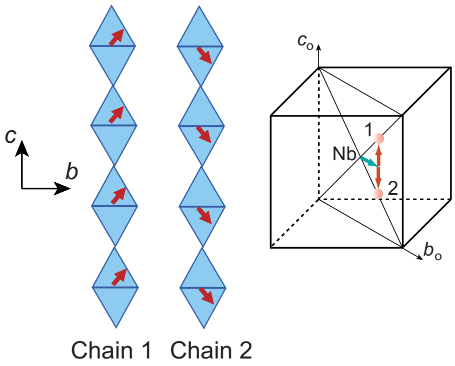

FIG. 8. (Color online) (Left) Schematic of the chainlike correlations for the local Nb displacements directed along $[111]_c$ and $[11\bar{1}]_c$; (right) A random mixture of chains 1 and 2 is equivalent to average Nb displacements along the $[110]_c$ direction (i.e., *b* axis) with additional disordered local-displacement components along the $[001]/[00\bar{1}]$ (i.e., *c* axis) directions. These chain correlations generate the $(00l)_o$ sheets of diffuse intensity observed in Fig. 7.

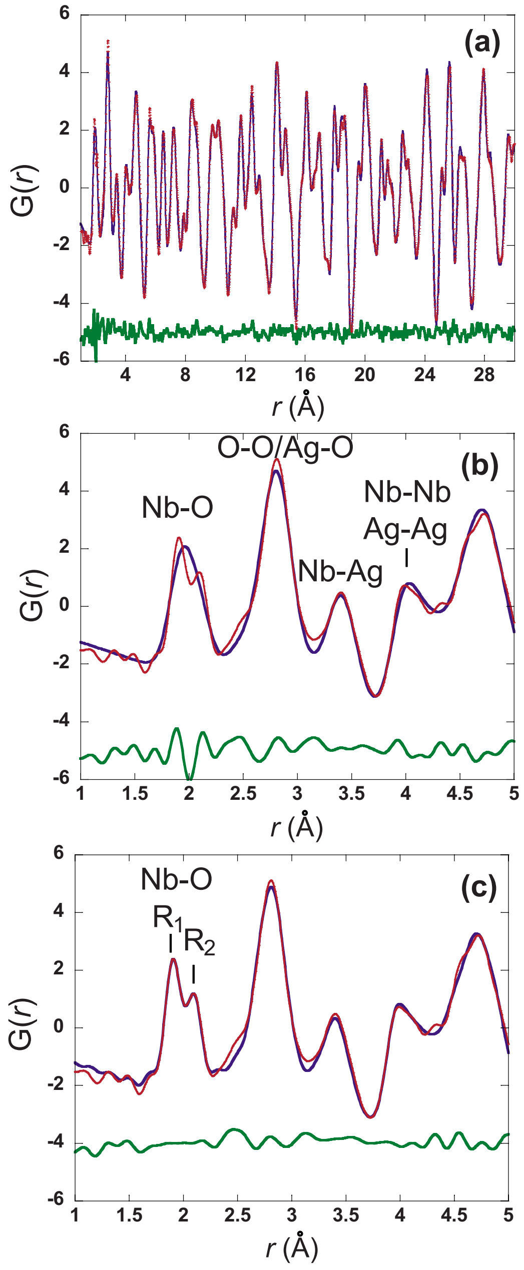

FIG. 9. (Color online) (a) Experimental (red) and calculated (blue) atomic PDF obtained from total neutron scattering at room temperature. (b) Low-*r* portion of the PDF in (a). The calculated PDF corresponds to the average structure refined from the Bragg profile. The calculated PDF matches the experimental data well at larger interatomic distances (a) but evidently fails to reproduce the first Nb-O peak (b). This peak can be recovered through additional refinements of the Nb atomic coordinates and anisotropic displacement parameters (c). The refined parameters exhibit a strong preference for Nb displacements along the *c* axis in addition to the average *b*-axis displacements. This result supports the model inferred from the electron-diffraction data (Fig. 8).

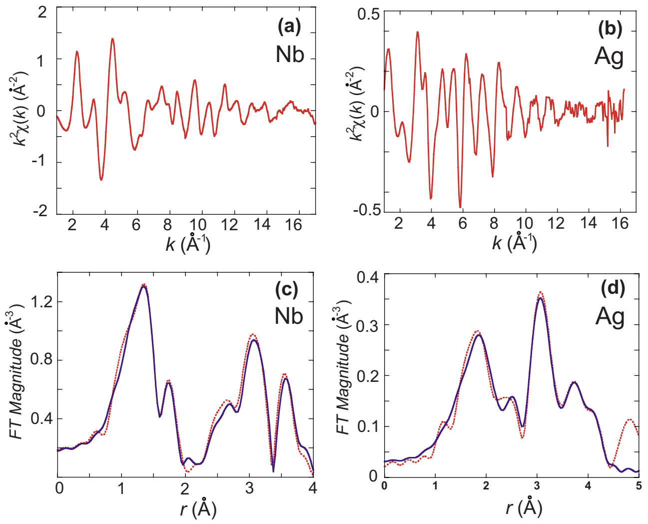

FIG. 10. (Color online) (a) and (b) Room-temperature Nb (a) and Ag (b) EXAFS data. (c) and (d) Experimental (red) and fitted (blue) magnitudes of the EXAFS Fourier transform for Nb and Ag. The k ranges used in the Fourier transforms were 2–15 Å^{-1} for Nb and 1.7–11.7 Å^{-1} for Ag. Prior to transform, the data were multiplied by the Hanning window ($dk=1$). Satisfactorily agreement between the experimental and calculated data was obtained by simultaneous fitting of both the Ag and Nb data sets using a model that included a two-shell Nb-O (3+3), a single-shell Nb-Ag, a single-shell Nb-Nb, a three-shell (3+6+3) Ag-O, and a two-shell Ag-Ag coordination. For each shell, an interatomic distance and its associated Debye-Waller factor were refined. Multiple-scattering contributions to the Nb EXAFS data were taken into account by introducing the Nb-O-Nb angle as an independent variable (this angle is determined primarily by octahedral tilting). We calculated multiple-scattering amplitudes for the three values of the Nb-O-Nb angle and used quadratic interpolation during the fit. All refined structural parameters acquired physically reasonable values.

the temperature dependence of the 220_o d spacing reveals anomalies that can still be associated with the $M_3 \leftrightarrow M_2$ (260 °C) and $M_2 \leftrightarrow M_1$ (75 °C) structural changes (Fig. 14). An additional, hitherto unsuspected, anomaly is also observed at ≈200 °C. The unit-cell volume of $AgNbO_3$ exhibited nearly linear positive thermal expansion (Fig. 15).

Simulations of x-ray diffraction patterns for the *Pbcm* structure indicate that the intensities of most superlattice reflections (e.g., 313_o, 304_o) are determined primarily by the Nb and Ag displacements and, therefore, can be used to

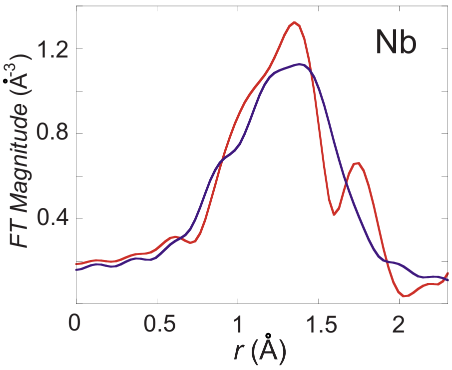

FIG. 11. (Color online) A single-shell fit of the EXAFS Nb-O peak at room temperature [$R_{\text{Nb-O}}=1.98(1)$ Å, $\sigma^2=0.017(3)$ Å^2]. The discrepancy between the experimental (red) and fitted (blue) data is considerably worse than that for a two-shell fit (Fig. 10).

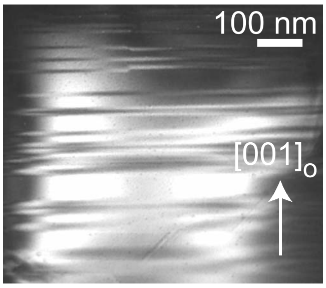

FIG. 12. Representative dark-field TEM image recorded with the 241-like reflections strongly excited near the $[\bar{2}10]_o$ orientation. A high incidence of antiphase domain boundaries aligned perpendicular to the $[001]_o$ direction is observed.

monitor their evolution with temperature. Indeed, the temperature dependence of the combined integrated intensities for the 313_o and 304_o reflections (Fig. 16) exhibits several anomalies that can be correlated with those for the 220_o d spacing. In particular, a strong increase in the slope is observed at ≈275 °C as well as the weak but discernible discontinuities at ≈200 and ≈75 °C. Thus, the structural changes that give rise to the anomalies in the 220_o d spacings appear to involve the cation displacements.

The temperature dependencies of key average-structure characteristics obtained from the refinements using neutron-diffraction data are summarized in Fig. 17. The angles that describe rotations of $[\mathrm{NbO}_6]$ octahedra about the b and c axes are designated as θ and ϕ, respectively (Fig. 18). Both angles [Figs. 17(c) and 17(d)] as well as the displacements of Nb [Fig. 17(a)] and Ag1 [Fig. 17(b)] from their ideal positions increase on cooling. All of these characteristics exhibit discernible anomalies at ≈200 °C. For the Ag1 displacements, additional pronounced changes are observed at ≈250 and ≈75 °C. A significant distortion of the $[\mathrm{NbO}_6]$ octahedra occurs on cooling. The distortion is accompanied by the progressive contraction of the apical [Fig. 17(e); Fig. 18] and expansion of the equatorial [Figs. 17(f) and 17(g); Fig. 18) O-O distances. This distortion increases notably below ≈250 °C [Fig. 17(e)] causing anomalous changes in the temperature dependencies of both 220 and 008 d spacings. The equatorial O-O distances exhibit pronounced changes at both 250 and 200 °C. The octahedral distortion correlates with the anomalous behavior of the Nb ADPs (Fig. 19): U_{33} exhibits an unusual maximum at ≈225 °C, while the ratio U_{22}/U_{33} decreases rapidly on cooling to 250 °C but remains constant below this temperature. Thus, the anomalies in both the 220_o and 008_o d spacings near the supposed $\mathrm{M}_3 \rightarrow \mathrm{M}_2$ transition (≈250 °C) can be attributed to the onset of octahedral distortion which, in turn, appears to be linked to changes in the anisotropy of the Nb ADPs. The average Nb-O distances in the ab plane exhibit anomalies at 200 and 75 °C which are consistent with the behavior of the average Nb displacements (Fig. 20). The dependence of the Nb-O distances along the c axis on temperature was weak and noisy because of the relatively large standard error for the z-axis component of the Nb displacements. For the Ag2 sublattice, the most significant effect is observed for the U_{22} component [Fig. 17(h)] which drops sharply below 100 °C thereby suggesting a partial displacive ordering on these sites.

Electron diffuse scattering exhibits a major qualitative change between 100 and 200 °C manifested in the appearance of diffuse $(h00)_c$ and $(0k0)_c$ relplanes (Fig. 21) in addition to the already present $(00l)_c$. This change in the diffuse scattering was accompanied by the drop in the integrated intensity of the superlattice reflections (Fig. 22) dominated by the cation displacements (e.g., 218_o, Fig. 21). Coexistence of the $(00l)_c$, $(h00)_c$, and $(0k0)_c$ diffuse sheets above T_f ≈175 °C can be readily attributed to the presence of the Nb local $\langle 001\rangle_c$-displacement correlations along the Nb-Nb-Nb chains parallel to all three orthogonal $\langle 001\rangle_c$ directions. Further heating caused an abrupt M→O transition at T ≈400 °C. In the O phase, sharp $hk\frac{1}{4}l_c$ reflections associated with the $(a^-b^-c^-)/(a^-b^-c^+)$ tilting in the M-phase were replaced with the diffuse relrods parallel to the c axis of the M structure [Fig. 21(d), indicated using dotted line]. These relrods likely reflect a strong disorder in the sign of octahedral rotations, which is consistent with the previous electron- and

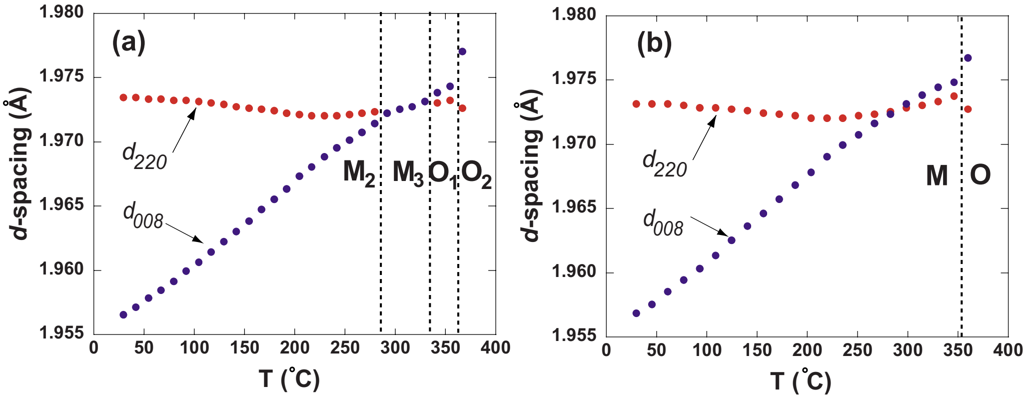

FIG. 13. (Color online) Temperature dependencies of the 220_o and 008_o d spacings: (a) results of the profile fitting to the $002_c=220_o+008_o$ reflection(s), (b) calculated from the lattice parameters obtained through Rietveld refinements. The uncertainties are within the symbol size. The results presented in (a) are consistent with literature reports and the changes can be associated with the previously reported phase-transition sequence $\mathrm{M}_2 \leftrightarrow \mathrm{M}_3 \leftrightarrow \mathrm{O}_1 \leftrightarrow \mathrm{O}_2$. In contrast, the results obtained using Rietveld refinements (b) indicate only the O↔M transition. Apparently, the measurement resolution was insufficient to resolve directly a small splitting of the 220_o and 008_o reflections in (a).

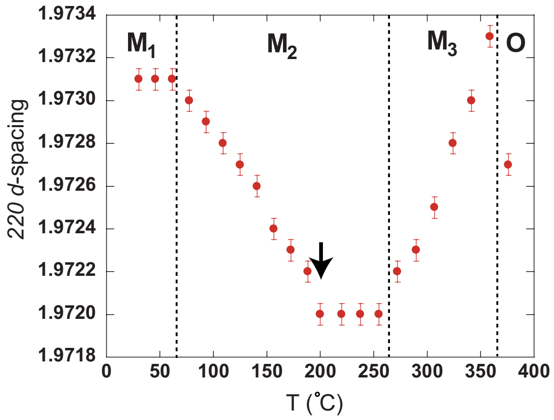

FIG. 14. (Color online) Magnified view of the temperature dependence of the 220_o d spacing. Several anomalies are clearly observed that can be correlated with the temperatures previously reported for the $M_1 \leftrightarrow M_3 \leftrightarrow M_3 \leftrightarrow O$ transitions. An additional anomaly occurs at ≈200 °C.

neutron-diffraction studies of AgNbO$_3$.[11,23] The diffuse scattering in the form of $\{h00\}_c$ relplanes is still present in the O phase. Unfortunately, at temperatures around ≈400 °C, AgNbO$_3$ starts to decompose under electron-beam irradiation in a TEM vacuum as manifested by the formation of nanoscale Ag precipitates. This problem has been well documented in the literature[23] and it renders any reliable TEM analyses of the high-temperature AgNbO$_3$ polymorphs unfeasible.

2. EXAFS and PDF

Consistent with the electron- and neutron-diffraction data, variable-temperature EXAFS (Fig. 23) revealed discontinuous changes for both Nb and Ag between 150 and 200 °C. An additional discontinuity is observed for Ag around 350 °C. Simultaneous fitting of the EXAFS data for Nb and Ag was conducted for a series of temperatures through the M-phase transitions. For all temperatures, fitting the Nb-O peak required a double (3+3) shell which suggests that this local Nb coordination is maintained even above the M↔O transition. Figure 24 displays a plot of the refined Nb-O distances, R_1 and R_2, as a function of temperature. A single anomaly is observed between 150 and 200 °C, as manifested in the small but significant discontinuity in the Nb-O distances on cooling; the simultaneous contraction of both the R_1 and R_2 distances on cooling implies the existence of pronounced correlations among the local Nb and O displacements. The discontinuity in the local Nb-O distances correlates with the change in electron diffuse scattering that occurs in the same temperature range.

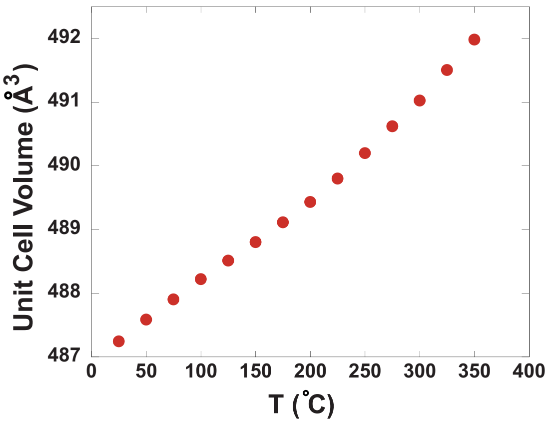

FIG. 15. (Color online) Temperature dependence of the unit-cell volume for AgNbO$_3$.

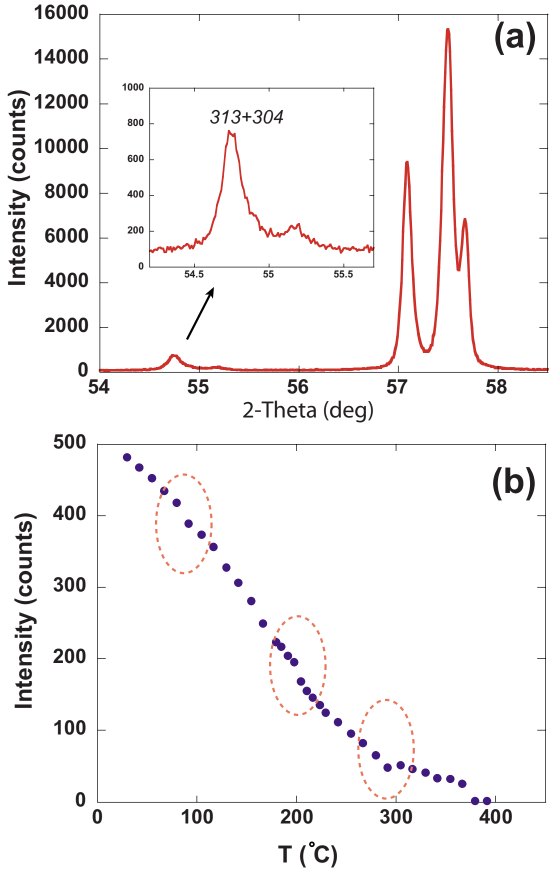

FIG. 16. (Color online) (a) A portion of the x-ray diffraction pattern displaying weak 313_o and 304_o superlattice reflections with intensities determined largely by the Nb and Ag displacements. (b) Temperature dependence of the combined integrated intensity for these reflections. The dependence reveals several anomalies at the same temperatures as observed for the 220_o d spacing in Fig. 12.

Unfortunately, trends in the EXAFS-refined parameters for the three Ag-O coordination shells were not as systematic as those for the Nb-O because of the relatively large number of variables needed to describe the highly distorted Ag coordination; additionally, the situation is complicated by the presence of Ag on the two symmetrically distinct sites. Thus, Ag EXAFS was used only as a qualitative indicator of changes in the local Ag coordination. A concurrent effect of Nb ordering on the Ag coordination at 200 °C can be ascribed to an expansion of the equatorial dimensions of the [NbO$_6$] octahedra which accompanies the Nb displacements. The anomaly near 350 °C can be attributed to the M→O tilting phase transition which is expected to primarily affect the Ag coordination sphere.

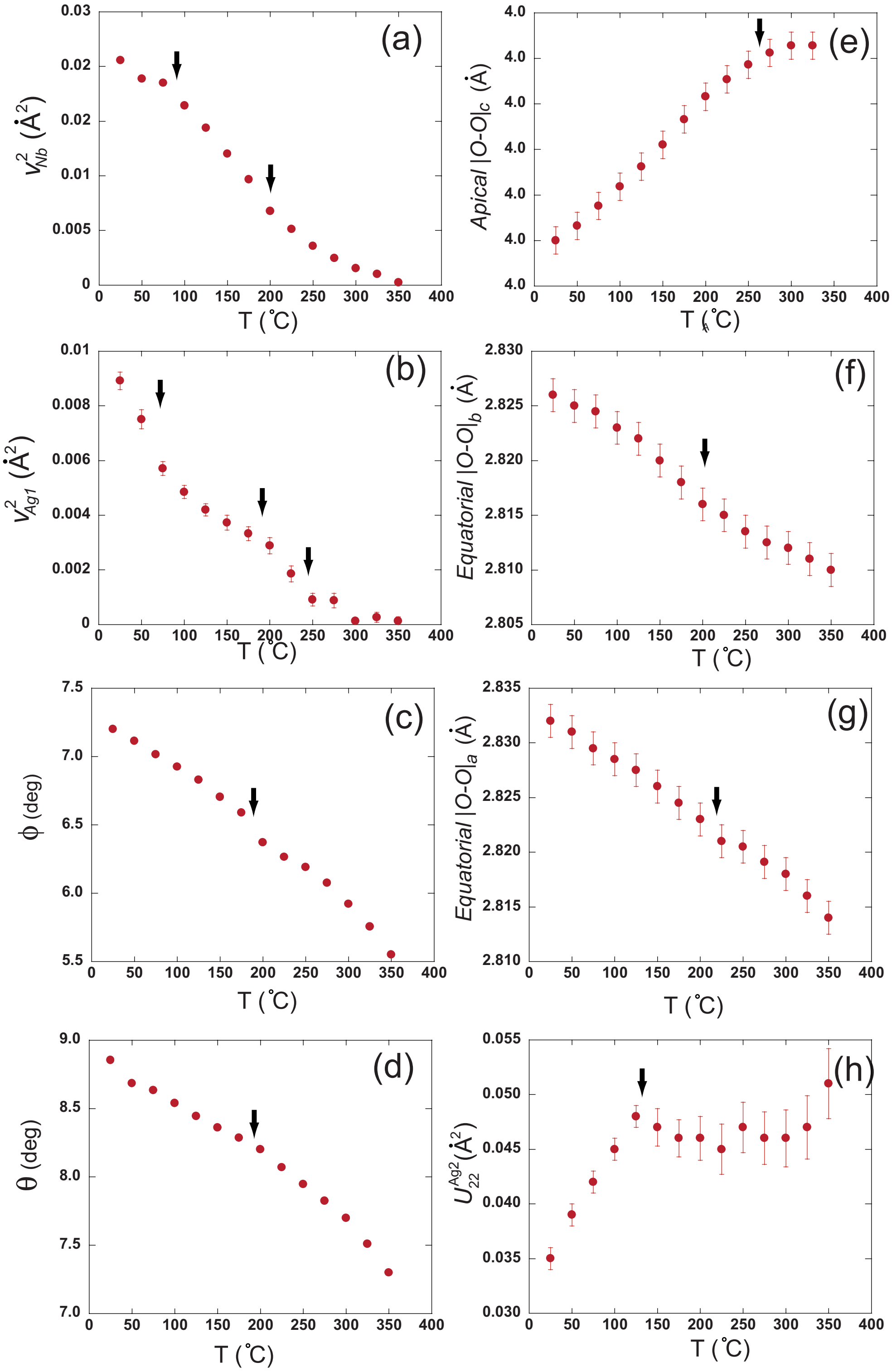

FIG. 17. (Color online) Temperature dependencies of several key structural characteristics obtained from Rietveld refinements using neutron-diffraction data. (a) Squared *b*-axis component, v^2_{Nb}, of the Nb displacements from the ideal $\frac{3}{4}\frac{3}{4}\frac{5}{8}$ positions, (b) Squared *b*-axis component, v^2_{Ag}, of the Ag1 displacements for the ideal $\frac{3}{4}\frac{1}{4}\frac{1}{2}$ positions, (c) ϕ tilting angle about *c* axis, (d) θ tilting angle about *b* axis, (e) apical O-O distance along the *c* axis (see Fig. 16 for description), (f) equatorial O-O distance along the *b* axis (Fig. 16), (g) equatorial O-O distance along the *a* axis (Fig. 16), (h) U_{22} component of the Ag2 atomic displacement parameters. The uncertainty for the Nb displacements in (a) is within the symbol size. Values of ϕ (c) and θ (d) were estimated from the oxygen coordinates. The uncertainties of these parameters are small as reflected in the low point-to-point noise of their temperature dependencies. The error bars shown for the |O-O| distances [(e)–(g)] were estimated by GSAS; the actual uncertainties appear to be much smaller as inferred from the low point-to-point noise in the temperature dependencies of these distances.

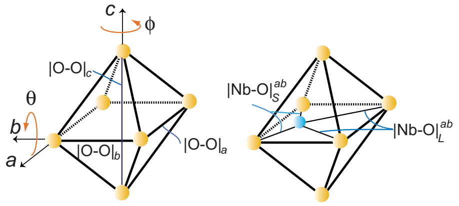

FIG. 18. (Color online) Schematics illustrating the definition of the ϕ and θ tilting angles and the O-O and Nb-O distances extracted from the average-structure refinements. The O-O distances are plotted in Fig. 15(e)–15(g), whereas the Nb-O distances are displayed in Fig. 18.

As found using EXAFS data, the Nb-O double peak in the neutron PDF collected at several temperatures across the M-phase field is consistent with $a \approx (3+3)$ Nb coordination (Fig. 25). Likewise, the PDF-derived $\Delta R = R_1 - R_2$ values and the D-W factors agree well with those obtained from EXAFS. The reproducibility of the present neutron PDF data was not sufficient to ascertain small (≈ 0.02 Å) discontinuities in the temperature trends of interatomic distances as suggested by EXAFS measurements. A reliable comparison of the coordination numbers as a function of temperature using a Gaussian fit to the Nb-O peak also was hindered by the small yet significant variances in the low-r ripples among the different data sets (Fig. 25). Nevertheless, the PDF data (Fig. 25) revealed a noticeable systematic change for the Ag-Nb peak that appears single for $T < 125$ °C but splits into a doublet for $T > 125$ °C; this change was not evident in EXAFS data (Fig. 23). Simulations indicate that the r-space resolution for the Ag EXAFS data, where the Ag-Nb peak is well isolated from the other coordination shells, might have been insufficient to observe this split. The split disappears near the temperature at which, according to Rietveld refinements, some ordering of the Ag2 displacements occurs.

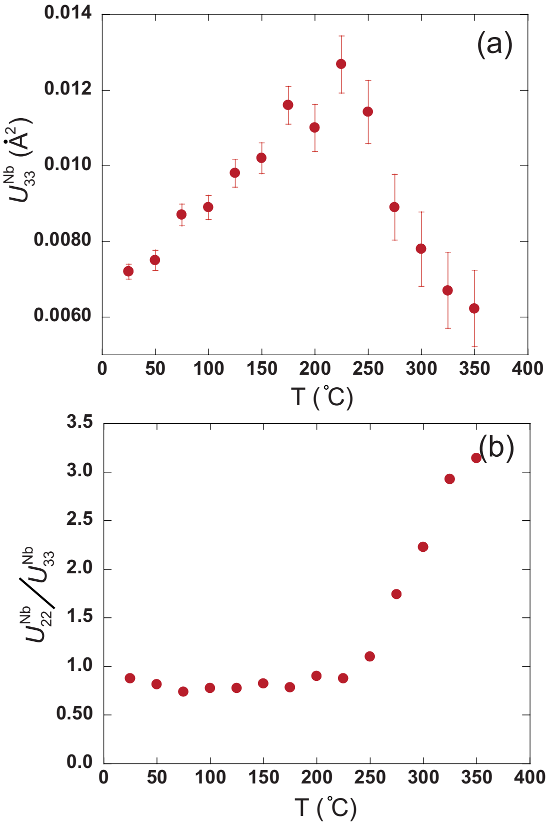

FIG. 19. (Color online) Temperature dependences of the U_{22} (a) and U_{22}/U_{33} (b) parameters for the Nb atoms. The uncertainties represent estimated standard deviations as calculated using GSAS.

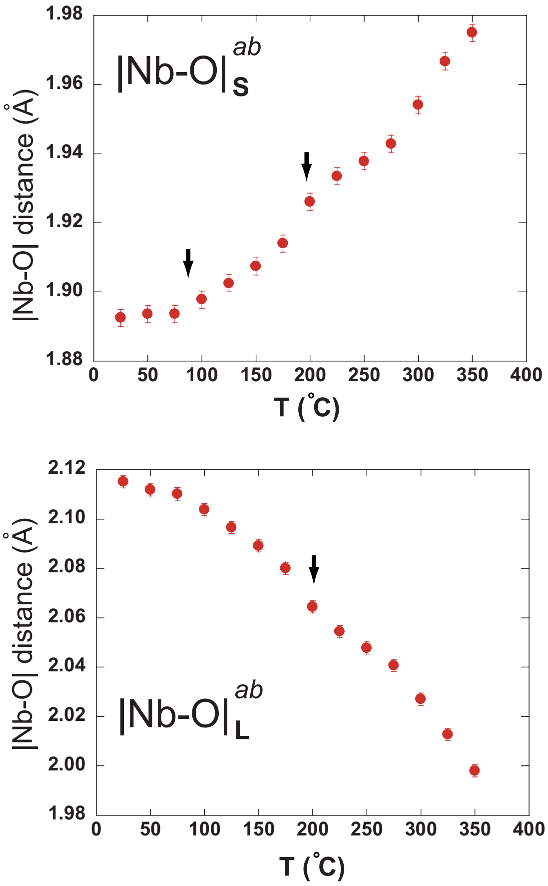

FIG. 20. (Color online) Temperature dependence of the average Nb-O distances in the *ab* plane as described in Fig. 16. The two different Nb-O distances are defined in Fig. 16.

IV. DISCUSSION

Overall, our results indicate the existence of intricate coupling between octahedral-tilting and local displacements of both Ag and Nb. These interactions trigger a series of changes in the cation displacements across the M-phase field. The coupling appears to be stronger for the [NbO$_6$] ϕ tilting about the c axis, and all major average-structure effects occur in the *ab* plane.

The presence of three sets of $\{100\}_c$ diffuse relplanes in the O phase, combined with EXAFS data, suggest that the Nb cations exhibit local off-center displacements above the M$\leftrightarrow$O transition while still residing, on average, at their ideal fixed-coordinate positions. In a cubic perovskite structure, a superposition of the three sets of orthogonal $\langle 001 \rangle_c$ chain-correlated displacements which give rise to diffuse

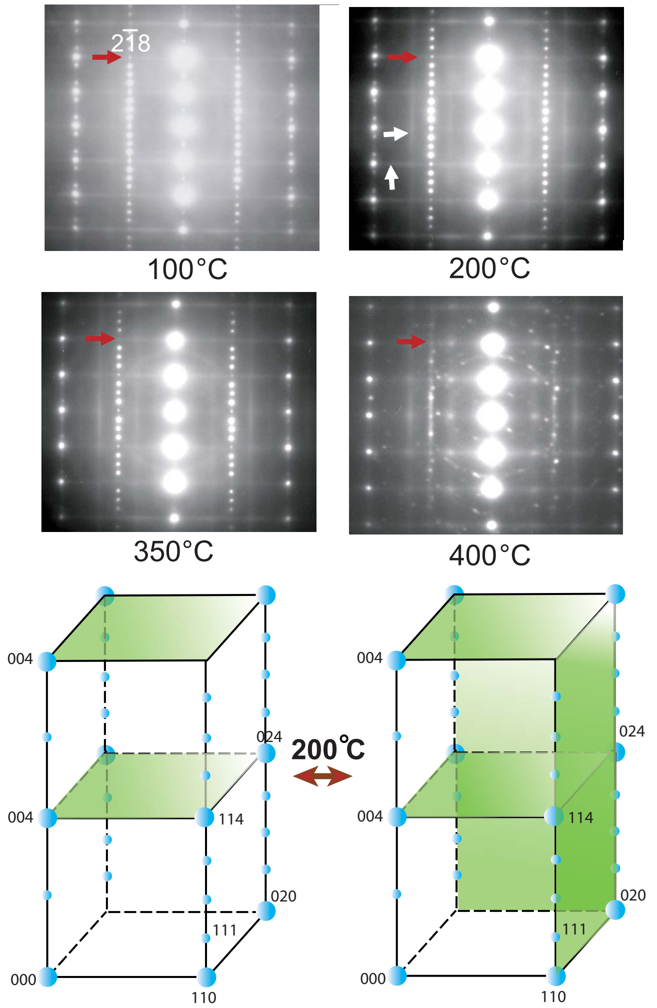

FIG. 21. (Color online) Variable-temperature electron-diffraction patterns recorded from a single domain of $AgNbO_3$ along the $\langle 103\rangle_c$ orientation. For $T > 175$ °C, two sets of diffuse streaks (i.e., vertical and horizontal) were observed, whereas for $T < 175$ °C one of these sets (horizontal) largely disappeared. A three-dimensional (3D) reconstruction of the changes in the diffuse intensity distribution is illustrated by the schematic drawing of the reciprocal lattice. The diffuse intensity sheets are highlighted. Around 400 °C, the superlattice reflections $hk\frac{1}{4}l_c$ associated with the $(a^-b^-c^-)/(a^-b^-c^+)$ octahedral tilting are replaced by the diffuse streaks (outlined using a dotted line). Numerous random spots and a ring that appear in the diffraction pattern at this temperature arise from precipitation of the nanoscale metallic Ag. The intensity of the 218_o reflection indicated using red arrows is determined primarily by the cation displacements. The temperature dependence of the intensity of this reflection is shown in Fig. 20.

sheets in diffraction is equivalent to local B-cation displacements along one of the eight $\langle 111\rangle_c$ directions. Such eight-site displacive disorder reportedly occurs in the cubic phases of $BaTiO_3$ and $KNbO_3$.[20] Our local-structure data for $AgNbO_3$ can also be interpreted by assuming a similar model for Nb displacements in the O phase. Conceivably, this eight-site displacive disorder is present even in the higher-temperature T and C polymorphs of $AgNbO_3$, but verification of this was beyond the scope of the present study.

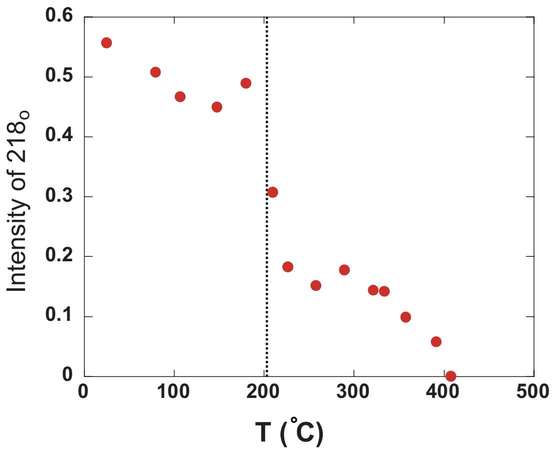

FIG. 22. (Color online) Temperature dependence of the integrated intensity of the 218_o reflection (indicated using red arrow in Fig. 19) which is determined entirely by the Ag and Nb displacements. A marked discontinuity in this dependence occurs in the same temperature range where the change in the electron diffuse scattering is observed.

The O → M phase transition, accompanied by the onset of $(a^-b^-c^-)/(a^-b^-c^+)$ octahedral tilting, removes the symmetry restrictions that constrain Nb to the average ideal positions, thereby promoting partial ordering of the local Nb displacements. In the average structure, this ordering is manifested by finite displacements of Nb that increase monotonically in magnitude with decreasing temperature; in fact, these displacements represent the order parameter. A combination of the *b*- and *c*-axis $[NbO_6]$ rotations generates significant lattice distortion, with $a < b$, which appears to stabilize average Nb displacements along the *b* axis. This ordering spans a

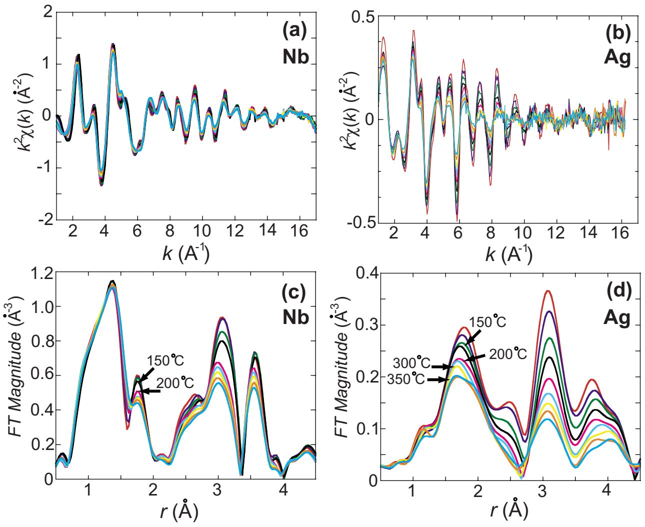

FIG. 23. (Color online) Variable-temperature Nb and Ag EXAFS k^2-weighted data [(a) and (b)] and their Fourier transforms [(c) and (d)] recorded between 25 and 400 °C. The *k* ranges used in the Fourier transforms were from 2 to 15 Å^{-1} for Nb and from 1.7 to 11.7 Å^{-1} for Ag. Prior to transform, the data were multiplied by the Hanning window ($dk = 1$). Both Nb and Ag EXAFS exhibit anomalies between 150 and 200 °C. For the Ag EXAFS, an additional anomaly between 300 and 350 °C can be observed.

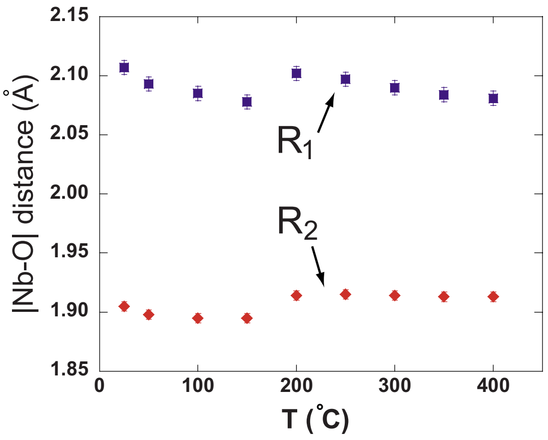

FIG. 24. (Color online) Local Nb-O distances (R_1 and R_2) obtained by fitting the EXAFS data. A (3+3) Nb coordination by O was assumed.

broad temperature range as inferred from the presence of the three sets of diffuse-scattering sheets down to $\approx$175 °C. As the ordering progresses, Nb still remains distributed among the eight sites but the site occupancies become nonequal (Fig. 26). The *Pbcm* symmetry, imposed by tilting, restricts average Nb displacements to the patterns depicted in Fig. 1. According to our model, the Nb cations in the *c* layers I and II preferentially occupy two (out of eight) sites displaced along the $[11l]$ and $[11\bar{l}]$ $(l \leq 1)$ directions, whereas those in the *c* layers III and IV favor sites displaced along the $[\bar{1}1l]$ and $[\bar{1}1\bar{l}]$; yet, the occupancy probabilities for the other six sites in each layer remain nonzero (Fig. 26).

The anomalous behavior of the U_{33} parameter for Nb (Fig. 19) can be interpreted by assuming a gradual rotation of the local atomic displacements below $T \approx 250$ °C; that is, the l index for the $[11l]$ displacement direction decreases with decreasing temperature. This rotation of the Nb displacements is consistent with the more rapid contraction of the apical distances and expansion of the equatorial distances for $T < 250$ °C. Such enhanced distortion of the $[NbO_6]$ octahedra appears to be responsible for the anomalies in the 220_o and 008_o *d* spacings which have been associated with the $M_2 \leftrightarrow M_3$ transition. Rotation of the displacement directions, as suggested by our data, also fits the so-called "spherical model" previously proposed to describe the behavior of B-cation displacements in perovskite-like zirconates.[24]

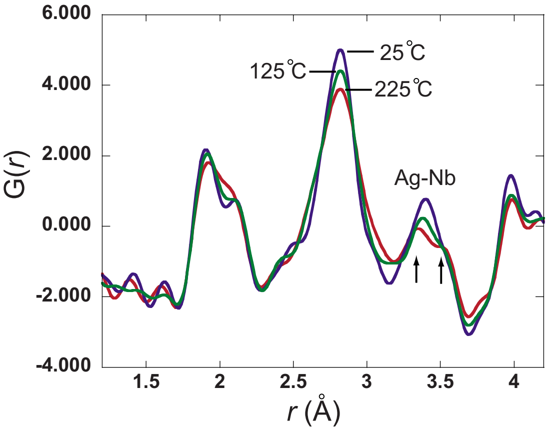

FIG. 25. (Color online) Low-*r* portions of the PDF at 25, 125, and 225 °C. Note a splitting of the Ag-Nb peak at higher temperatures (indicated using arrows).

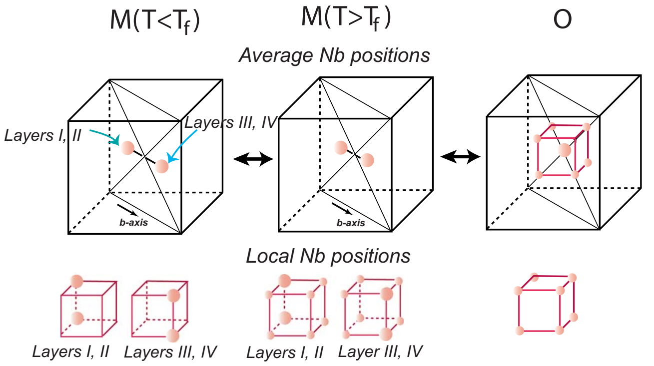

FIG. 26. (Color online) Schematic for the Nb order-disorder behavior as a function of temperature. In the O phase, Nb atoms occupy ideal average positions but are locally disordered among the eight sites displaced along $\langle 11l \rangle_c$ $(l \leq 1)$ directions. In the M phase, the Nb cations become partially ordered with average displacements along the *b* axis. Locally, above $T_f \approx 175$ °C, Nb still remains distributed among the eight sites but the site occupancies become nonequal as indicated using differently sized spheres. In particular, the Nb cations in the *c* layers I and II preferentially occupy two sites displaced along the $[11l]$ and $[11\bar{l}]$ directions, whereas those in the *c* layers III and IV favor sites displaced along the $[\bar{1}1l]$ and $[\bar{1}1\bar{l}]$. The occupancy probabilities for the other six sites decrease gradually with decreasing temperature and vanish below T_f.

For $T < 175$ °C, both the $(h00)_c$ and $(0k0)_c$ sets of diffuse relplanes essentially disappear, signifying a transition from eight-to-two-site Nb disorder in each *c* layer, as illustrated in Fig. 26. Note that the average *Pbcm* symmetry is maintained upon this change. The evolution of the diffuse scattering on cooling in $AgNbO_3$ resembles the consecutive disappearance of the $(h00)$, $(0k0)$, and $(00l)$ diffuse sheets in $BaTiO_3$ and $KNbO_3$ upon their series of the cubic → tetragonal → orthorhombic → rhombohedral phase transitions.[20]

The ordering of Nb displacements appears to affect both the oxygen and Ag sublattices. The coupling between the Nb and Ag sublattices presumably occurs through the oxygen atoms. According to our results, the progressive increase in the average Nb displacements on cooling is accompanied by expansion of the $[NbO_6]$ octahedra in the *ab* plane which affects the Ag coordination and enhances the magnitude of octahedral rotations. Concurrently, octahedral tilting brings the centers of the $[NbO_6]$ octahedra closer together, which increases the repulsive forces between the Nb-Nb and Nb-Ag next-nearest neighbors and may also support expansion of the $[NbO_6]$ units. A balance between these two effects determines the overall changes in the lattice parameters. The exact reasons for the expansion of both equatorial dimensions in the $[NbO_6]$ octahedra remain unclear and deserve theoretical investigation.

Our results combined with the previously published data on $KNbO_3$ and $NaNbO_3$ suggest a general tendency for Nb disorder in $ANbO_3$ perovskites over sites displaced off center along the $\langle 111\rangle_c$ directions. Similar ideas have been expressed by Ivliev *et al.*[25] from their dielectric and EXAFS measurements on $KNbO_3$ and $NaNbO_3$. In the absence of octahedral tilting in $KNbO_3$, ordering of Nb displacements gives rise to a sequence of well-defined phase transitions accompanied by reduction in the average symmetry. Common tilt systems, such as $a^0a^0c^-$, $a^0a^0c^+$, or $a^+b^-b^-$, constrain B cations to reside on the high-symmetry fixed-coordinate positions and therefore preclude ordering of Nb displacements. In contrast, rhombohedral tilting $a^-a^-a^-$ is compatible with $\langle 111\rangle_c$ cation displacements and therefore supports the development of polar order on the Nb sites, as indeed observed for $NaNbO_3$, which undergoes a ferroelectric $Pbcm \leftrightarrow R3c$ phase transition at 173 K.[6] The $(a^-b^-c^-)/(a^-b^-c^+)$ tilting in the room-temperature polymorphs of $AgNbO_3$ and $NaNbO_3$ creates an intermediate case as it allows for a *partial* ordering of Nb displacements in an antipolar array. This ordering within the *Pbcm* structure does not affect the average symmetry because the Nb atoms occupy nonsymmetric (x, y, z) positions and, therefore, no well-defined phase transition occurs. The structural states previously attributed to the M_3 and M_2 phases appear to represent different stages of partial cation ordering within the same *Pbcm* symmetry rather than distinct phases in a thermodynamic sense.

The $M_2 \rightarrow M_1$ transition in $AgNbO_3$ is reportedly ferroelectric with a weak spontaneous polarization in the M_1 structure.[26] In principle, a spontaneous polarization could develop if the Nb cations in all c layers preferentially occupy positions displaced along either the $[11l]$ or $[11\bar{l}]$ directions thereby reducing the symmetry from the *Pbcm* to $Pbc2_1$. This change is difficult to ascertain because the deviations from mirror symmetry are expected to be small. For example, neutron refinements provided no evidence for a loss of inversion symmetry down to 1.5 K.[11] Our EXAFS, Rietveld refinements, and PDF data suggest that partial ordering of the Ag2 displacements along the b axis occurs in the vicinity of the supposed $M_2 \rightarrow M_1$ transition. Some concurrent changes in the Nb and Ag1 displacements occur around this temperature as well (Fig. 17). Yet, the exact structural changes associated with the $M_2 \leftrightarrow M_1$ transition still remain unclear because of their subtlety. Reverse Monte Carlo (RMC) local-structure refinements enable explicit treatment of atomic disorder and, in principle, could provide some insight into a possible order-disorder behavior on the Ag sublattices. Our RMC refinements using simultaneous real- and reciprocal-space fittings of the neutron total scattering data yielded a good fit to both experimental data sets but failed to reproduce the diffuse scattering in electron diffraction. More elaborate RMC refinements that incorporate both total scattering data and Ag and Nb EXAFS data under the restraints imposed by electron diffraction are in progress and, if successful, will be reported separately.

Previous studies which combined dielectric, infrared, and Raman spectroscopy[12,13] identified a submillimeter relaxational mode as responsible for a diffuse peak of dielectric constant observed in the vicinity of the $M_3 \leftrightarrow M_2$ transition. The mode has been attributed to the Nb dynamics. Our present results are consistent with this interpretation. Order-disorder behavior on the Nb sublattice accompanied by rotations of displacement directions constitutes a plausible source for the high-frequency dielectric relaxation. Freezing of the two local-displacement components below the dielectric maximum temperature is also consistent with a relaxational nature of the broad dielectric peak. Conceivably, the $(a^-b^-c^-)/(a^-b^-c^+)$ octahedral tilting in systems with ferroelectrically active B cations (e.g., Nb, Ti) creates conditions favorable for achieving a high dielectric constant and modest dielectric losses by stabilizing a *partial* antipolar order of the B-cation displacements as opposed to the ordered antiferroelectric or ferroelectric states. Likewise, such partial ordering may facilitate voltage tunability of the dielectric constant.

As a next step, we plan to investigate the effect of Ta substitution on the local order/disorder behavior in $AgNbO_3$. Room-temperature Rietveld refinements of the commercially relevant $AgNb_{1/2}Ta_{1/2}O_3$ composition support the *Pbcm* model. Electron-diffraction patterns from these samples exhibit three sets of diffuse $\{100\}_c$ relplanes as observed for $AgNbO_3$ above 200 °C. Detailed analyses of local structure and phase transitions in $AgNb_{1/2}Ta_{1/2}O_3$ are in progress and will be reported elsewhere.

V. CONCLUSIONS

This study demonstrates that partial ordering of Nb displacements induced by coupling between $(a^-b^-c^-)/(a^-b^-c^+)$ octahedral-tilting and local polar Nb displacements dominates the structural behavior of the M phase of $AgNbO_3$. Similar to $KNbO_3$, disordered local off-center Nb displacements along the $\langle 11l\rangle_c$ $(l \leq 1)$ directions appear to be present even in the higher-temperature $AgNbO_3$ polymorphs. The $\langle 100\rangle_c$ components of these displacements are correlated along $\langle 100\rangle_c$ -Nb-Nb-Nb chains. The onset of $(a^-b^-c^-)/(a^-b^-c^+)$ octahedral tilting generates sufficient strain and distortion to promote long-range order of the Nb displacements; however, the *Pbcm* symmetry of the tilted octahedral framework is incompatible with complete ordering and, therefore, only a partial antipolar order is established. According to our results, both the M_3 and M_2 structures represent the same phase but exhibit different degrees of ordering. Order-disorder behavior on the Nb sublattice appears to give rise to high-frequency dielectric relaxation. This interpretation agrees with previous spectroscopic investigations of $AgNbO_3$. Additional positional disorder is observed for the Ag cations on the Ag2 sites as manifested by highly anisotropic atomic displacements parameters with large components along the b axis. The Ag2 local displacements appear to exhibit partial ordering below 100 °C. The contribution of Ag disorder to the dielectric relaxation remains to be established.

ACKNOWLEDGMENTS

The work was made possible by national user facilities: (1) the Lujan Center at Los Alamos Neutron Science Center funded by the Department of Energy Office of Basic Energy Sciences, and Los Alamos National Laboratory under Contract No. W-7405-ENG-36, and (2) the Advanced Photon Source supported by the Department of Energy Office of Basic Energy Sciences under Contract No. W-31-109-ENG-38. Experiments at the ISIS Pulsed Neutron and Muon Source were supported by a beam-time allocation from the Science and Technology Facilities Council.

---

[1] M. Valant, A. K. Axelsson, and N. Alford, J. Eur. Ceram. Soc. **27**, 2549 (2007).

[2] M. Valant, D. Suvorov, C. Hoffmann, and H. Sommariva, J. Eur. Ceram. Soc. **21**(15), 2647 (2001).

[3] J. Fabry, Z. Zikmund, A. Kania, and V. Petricek, Acta Crystallogr., Sect. C: Cryst. Struct. Commun. **56**, 916 (2000).

[4] A. M. Glazer, Acta Crystallogr., Sect. B: Struct. Crystallogr. Cryst. Chem. **28**, 3384 (1972).

[5] A. C. Sakowski-Cowley, K. Lukaszewicz, and H. D. Megaw, Acta Crystallogr., Sect. B: Struct. Crystallogr. Cryst. Chem. **25**, 851 (1969).

[6] S. K. Mishra, N. Choudhury, S. L. Chaplot, P. S. R. Krishna, and R. Mittal, Phys. Rev. B **76**, 024110 (2007).

[7] R. Ranjan and D. Pandey, J. Phys.: Condens. Matter **13**, 4251 (2001).

[8] S. K. Mishra, R. Ranjan, D. Pandey, and H. T. Stokes, J. Phys.: Condens. Matter **18**, 1885 (2006).

[9] M. Pawelczyk, Phase Transitions **8**, 273 (1987).

[10] A. Ratuszna, J. Pawluk, and A. Kania, Phase Transitions **76**, 611 (2003).

[11] P. Sciau, A. Kania, B. Dkhil, E. Suard, and A. Ratuszna, J. Phys.: Condens. Matter **16**(16), 2795 (2004).

[12] W. Fortin, G. E. Kugel, J. Grigas, and A. Kania, J. Appl. Phys. **79**, 4273 (1996).

[13] J. Petzelt, S. Kamba, E. Buixaderas, V. Bovtun, Z. Zikmund, A. Kania, V. Koukal, J. Pokorny, J. Polivka, V. Pashkov, G. Komandin, A. Volkov, Ferroelectrics **223**, 235 (1999).

[14] Smaller amounts of excess Ag_2O in the raw mixture led to the second phase $Ag_2Nb_4O_{11}$, whereas larger concentrations left residual metallic Ag.

[15] A. C. Larson and R. B. von Dreele, LAUR Report No. 86–748, 1994 (unpublished).

[16] B. Ravel and M. Newville, J. Synchrotron Radiat. **12**, 537 (2005).

[17] S. I. Zabinsky, J. J. Rehr, A. Ankudinov, R. C. Albers, and M. J. Eller, Phys. Rev. B **52**, 2995 (1995).

[18] C. L. Farrow, P. Juhas, J. W. Liu, D. Bryndin, E. S. Bozin, J. Bloch, Th. Proffen, and S. J. L. Billinge, J. Phys.: Condens. Matter **19**, 335219 (2007).

[19] M. G. Tucker, D. A. Keen, M. T. Dove, A. L. Goodwin, and Q. Hui, J. Phys.: Condens. Matter **19**, 335218 (2007).

[20] R. Comes, M. Lambert, and A. Guinner, Solid State Commun. **6**, 715 (1968).

[21] F. A. Kassan-Ogly and V. E. Naish, Acta Crystallogr., Sect. B: Struct. Sci. **42**, 314 (1986).

[22] Y. Liu, R. L. Withers, X. Y. Wei, and J. D. F. Gerald, J. Solid State Chem. **180**, 858 (2007).

[23] M. Verwerft, D. Van Dyck, V. A. M. Brabers, J. Van Landuyt, and S. Amelinkx, Phys. Status Solidi A **112**, 451 (1989).

[24] R. V. Vedrinskii, E. S. Nazarenko, M. P. Lemeshko, V. Nassif, O. Proux, A. A. Novakovich, and Y. Joly, Phys. Rev. B **73**, 134109 (2006).

[25] M. P. Ivliev, S. I. Raevskaya, I. P. Raevskii, V. A. Shuvaeva, and I. V. Pirog, Phys. Solid State **49**, 769 (2007).

[26] A. Kania, K. Roleder, and M. Lukaszewski, Ferroelectrics **52**, 265 (1984).